



Effects of Ni²⁺ doping on the performances of lithium iron pyrophosphate cathode material



Jun-chao Zheng ¹, Xing Ou ¹, Bao Zhang ^{*}, Chao Shen, jia-feng Zhang, Lei Ming, Ya-dong Han

School of Metallurgy and Environment, Central South University, Changsha 410083, PR China

HIGHLIGHTS

- Ni doped Li₂Fe_{1-x}Ni_xP₂O₇/C composites were synthesized for the first time.
- Doping nickel at an appropriate amount could increase the Li⁺ diffusion coefficient.
- Ni doping is an effective way to improve the electrochemical performance of Li₂FeP₂O₇.

ARTICLE INFO

Article history:

Received 28 March 2014

Received in revised form

7 May 2014

Accepted 30 May 2014

Available online 9 June 2014

Keywords:

Lithium ion battery

Cathode material

Lithium iron pyrophosphate

Doping

Electrochemical performances

ABSTRACT

The Li₂Fe_{1-x}Ni_xP₂O₇/C ($x = 0.00, 0.02, 0.04, 0.06, 0.08, 0.10$) composites were successfully synthesized for the first time by a conventional solid state route. The solid state reaction mechanism, crystal structure, morphology, and electrochemical performance of the samples are characterized in detail. The XRD results show that Ni²⁺ is incorporated in the lattice of Li₂FeP₂O₇ and the monoclinic structure does not change after doping. Among all the samples, the Li₂Fe_{0.98}Ni_{0.02}P₂O₇/C composite delivers the highest discharge capacity of 110.2 mAh g⁻¹ at 0.025C, and possesses a capacity retention ratio of 90.1% after 100 cycles at 0.05C, demonstrating the best rate performance and cycle stability in the potential range of 2.0–4.5 V. Electrochemical impedance spectroscopy (EIS) results reveal that the Li₂Fe_{0.98}Ni_{0.02}P₂O₇/C sample has a lower charge transfer resistance and a higher Li-ion diffusion coefficient compared to other samples. The results indicate Ni²⁺-doping in Li₂FeP₂O₇/C can effectively enhance the electrochemical performance of this monoclinic compound, especially at a high charge/discharge rate.

© 2014 Elsevier B.V. All rights reserved.

1. Introduction

There are intensive research activities for alternative electrode materials in the next generation of rechargeable lithium ion batteries, particularly for those used in hybrid and pure electric vehicles [1–3]. Phosphate-based cathode materials have been a considerable investigation due to its attractive properties, such as low-cost, abundant iron and phosphate groups (PO₄) which are safer and more stable than layered transition-metal oxides (LiCoO₂) [4]. Among these compounds, most studies have been devoted to the development of olivine-structured LiFePO₄, the most commercially viable polyanionic cathode material with large-scale synthesis and competent capacity stability [5]. However, the

operating voltage of LiFePO₄ is relatively lower than LiMn₂O₄ and LiNi_{1/3}Co_{1/3}Mn_{1/3}O₂ which limits high practical energy density. Meanwhile, a myriad of polyanion-type compounds based on silicates (Li₂MSiO₄) [6], borates (LiMBO₃) [7], fluorosulfates (LiMSO₄F) [8], fluorophosphates (LiMPO₄F) [9] and hydroxysulfate (LiMSO₄OH) [10] have also received much attention. Nonetheless, many of them either suffer from low redox potential and discharge capacity, or difficult synthesis.

Since the monoclinic structure of lithium iron pyrophosphate (Li₂FeP₂O₇) was first reported by Nishimura [11] and his co-workers in 2010, it has captured the attention of researchers due to its higher reversible potential of 3.5 V vs. Li/Li⁺, which is the highest voltage among all Fe-containing phosphate cathodes [12]. Although the lack of safe high-voltage electrolytes and the structural instability make it difficult to detect that two lithium ions intercalate and deintercalate into the Li₂FeP₂O₇ cathode, its theoretical discharge capacity is in range of 2.0–4.5 V remains at 110 mAh g⁻¹ [12,13]. Contrast to 1D diffusion in LiFePO₄, Clark [14] predicted that

* Corresponding author. Tel.: +86 731 88836357.

E-mail address: jczheng@csu.edu.cn (B. Zhang).

¹ The authors (Jun-chao Zheng and Xing Ou) contributed equally to this work and should be considered co-first authors.

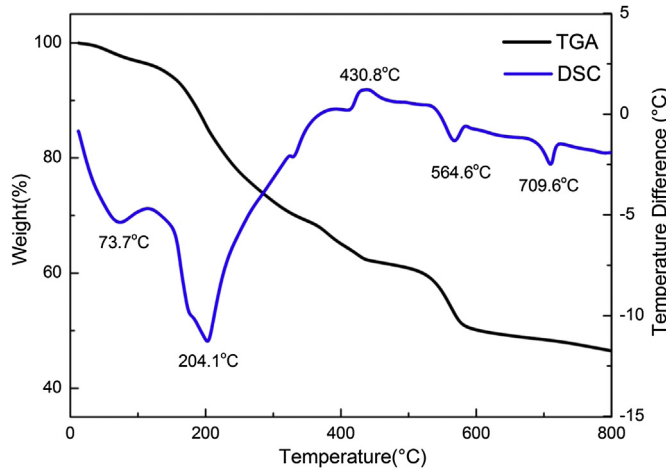


Fig. 1. TG–DSC curves of the $\text{Li}_2\text{Fe}_{0.92}\text{Ni}_{0.08}\text{P}_2\text{O}_7/\text{C}$ precursor.

$\text{Li}_2\text{FeP}_2\text{O}_7$ might have good rate capability due to fast Li^+ transportation through a 2D network in the bc-plane. However, the continuous research and commercial processing of $\text{Li}_2\text{FeP}_2\text{O}_7$ is mostly limited to its crystal structure and electrochemical performance.

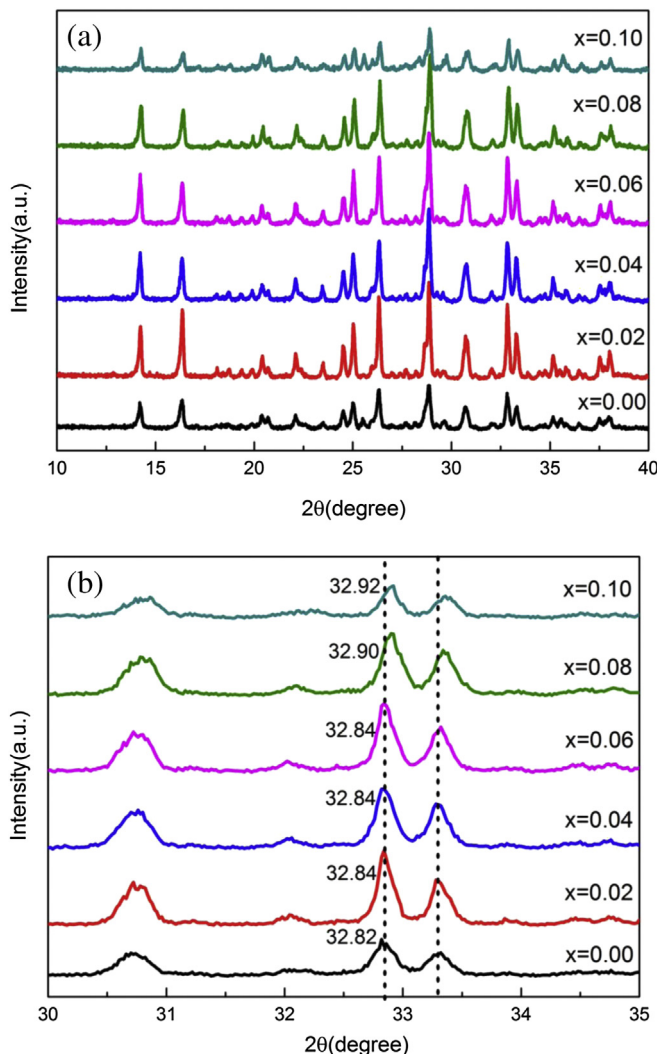


Fig. 2. (a)XRD patterns of $\text{Li}_2\text{Fe}_{1-x}\text{Ni}_x\text{P}_2\text{O}_7/\text{C}$ with various doping amount. (b)The magnification of the shift peaks of the XRD patterns.

Up until the present, various approaches have been proposed to optimize this new pyrophosphate, such as particle size reducing [15], metal ion doping [16] and carbon coating [15,17]. Compared with other methods, it is more reasonable to dope $\text{Li}_2\text{FeP}_2\text{O}_7$ with trace elements to increase the $\text{Fe}^{2+}/\text{Fe}^{3+}$ redox potential and stabilize the crystal structure without degrading its energy density. $\text{Li}_2\text{FeP}_2\text{O}_7$ has been doped with transition metals, such as Mn^{2+} [18–20], Co^{2+} [21,22], V^{5+} and Nb^{5+} [14]). Although Mahesh [23] studied the thermal, magnetic and impedance properties of $\text{Li}_2\text{NiP}_2\text{O}_7$, the electrochemical performance has not been mentioned.

In this paper, the pristine $\text{Li}_2\text{FeP}_2\text{O}_7/\text{C}$ and Ni doping of $\text{Li}_2\text{Fe}_{1-x}\text{Ni}_x\text{P}_2\text{O}_7/\text{C}$ ($x = 0.02, 0.04, 0.06, 0.08, 0.10$) composites have been synthesized by a conventional solid state route. The effect of Ni doping with different amounts on the crystal structure and electrochemical property of $\text{Li}_2\text{FeP}_2\text{O}_7/\text{C}$ are studied in detail for the first time.

2. Experimental

The $\text{Li}_2\text{Fe}_{1-x}\text{Ni}_x\text{P}_2\text{O}_7/\text{C}$ ($x = 0.02, 0.04, 0.06, 0.08, 0.10$) composites are prepared via conventional solid-state reaction by using LiH_2PO_4 (99.5% Aldrich), $\text{FeC}_2\text{O}_4 \cdot 2\text{H}_2\text{O}$ (99.0% Aldrich) and $\text{Ni}(\text{CH}_3\text{COO})_2 \cdot 4\text{H}_2\text{O}$ (99.0% Aldrich). The raw materials are mixed with glucose (99.5% Aldrich) in the weight ratio of 95:5, and ground in a ball mill (with a rotation speed of 300 r min^{-1} , agate balls) for 6 h in ethanol solution. After being dried at 80 °C, the mixture was then decomposed at 300 °C for 3 h, the resulting powder were then

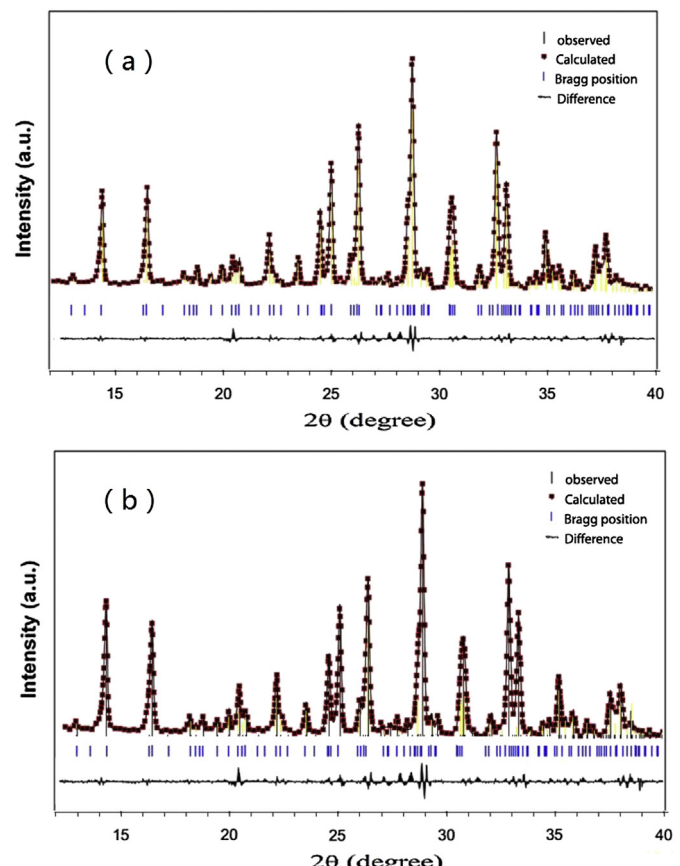


Fig. 3. Rietveld refinement of the XRD patterns of (a) $\text{Li}_2\text{FeP}_2\text{O}_7/\text{C}$ and (b) $\text{Li}_2\text{Fe}_{0.92}\text{Ni}_{0.08}\text{P}_2\text{O}_7/\text{C}$.

Table 1

Lattice parameters of the as-prepared composites.

Samples	$a(\text{\AA})$	$b(\text{\AA})$	$c(\text{\AA})$	$\beta(^{\circ})$	$V(\text{\AA}^3)$	$R_p(\%)$
$\text{Li}_2\text{FeP}_2\text{O}_7/\text{C}$	11.0329(8)	9.7601(5)	9.8166(9)	101.54(4)	1035.705	6.54
$\text{Li}_2\text{Fe}_{0.98}\text{Ni}_{0.02}\text{P}_2\text{O}_7/\text{C}$	11.0230(7)	9.7568(0)	9.8129(2)	101.56(6)	1033.962	6.38
$\text{Li}_2\text{Fe}_{0.96}\text{Ni}_{0.04}\text{P}_2\text{O}_7/\text{C}$	11.0229(8)	9.7545(7)	9.8110(7)	101.52(9)	1033.656	9.12
$\text{Li}_2\text{Fe}_{0.92}\text{Ni}_{0.08}\text{P}_2\text{O}_7/\text{C}$	11.0118(5)	9.7500(9)	9.8055(5)	101.54(9)	1031.487	8.3
$\text{Li}_2\text{Fe}_{0.90}\text{Ni}_{0.10}\text{P}_2\text{O}_7/\text{C}$	11.0091(8)	9.7503(1)	9.8052(2)	101.54(6)	1031.233	9.28
$\text{Li}_2\text{FeP}_2\text{O}_7^{\text{a}}$	11.0148(7)	9.7551(5)	9.7993(6)	101.491	1031.852	4.90
$\text{Li}_2\text{FeP}_2\text{O}_7^{\text{b}}$	11.0224(4)	9.7541(3)	9.8080(3)	101.564(2)	1033.083	3.28

^a Data taken from Ref. [16].^b Data taken from Ref. [22].

reground and sintered for 10 h at 650 °C in argon (99.999% in purity).

Thermogravimetric (TG/DSC) analysis of the mixture was measured on a SDT Q600 TG-DTA apparatus at temperatures between 25 and 800 °C at a heating rate of 5 °C min⁻¹ under argon flow. The powder X-ray diffraction (Rint-2000, Rigaku) measurement using Cu K α radiation was employed to identify the crystalline phase of the synthesized materials. The lattice parameter refinement and analysis was implemented in the Jade 9.0 Whole Pattern Fitting (WPF) program [24,25]. The Fourier transform infrared (FT-IR) spectrum was obtained by a Nicolet 460 FT-IR spectrophotometer. The samples were observed through SEM (JEOL, JSM-5600LV) and a Tecnai G12 transmission electron microscope (TEM). The X-ray photoelectron spectroscopy (XPS) measurements were carried on a K-Alpha 1063 spectrometer with a Mg K α achromatic X-ray source (1235.6 eV).

The electrochemical characterizations were performed using CR2025 coin-type cells. Typical positive electrode loadings were in the range of 2–2.5 mg cm⁻², and an electrode diameter of 14 mm was used. The electrodes were prepared by mixing as-prepared $\text{Li}_2\text{FeP}_2\text{O}_7$ with carbon black and polyvinylidene fluoride in a weight ratio of 80:10:10 in NMP. The separator is a Celguard2400

microporous polyethylene membrane. The electrolyte is 1 mol L⁻¹ LiPF₆ in a mixture of ethylene carbonate/dimethyl carbonate/ethylmethyl carbonate (EC/DMC/EMC) solution (1:1:1, volume ratio). A lithium metal anode is used in this study. The cells are assembled in a glove box filled with argon gas. The discharge–charge cycling is galvanostatically performed at 0.025C to 2C rates with cut-off voltages of 2.0–4.5 V (versus Li/Li $^{+}$) at room temperature, and the specific capacity of samples is evaluated based on the active materials. The cyclic voltammetric and EIS measurements were carried out with a CHI660D electrochemical analyzer. The CV curves for the above test cells were recorded in the potential range of 2.0–4.5 V. The impedance spectra were recorded by applying an AC voltage of 5 mV amplitude in the 100 KHz–0.1 Hz frequency range.

3. Results and discussion

In order to determine the appropriate calcination temperature, TG–DSC analysis of the $\text{Li}_2\text{Fe}_{0.92}\text{Ni}_{0.08}\text{P}_2\text{O}_7/\text{C}$ precursor was performed, as shown in Fig. 1. There are several stages of weight loss in the TG plot and corresponding endothermic/exothermic peaks in the DSC plot. From ambient temperature to 400 °C, the initial

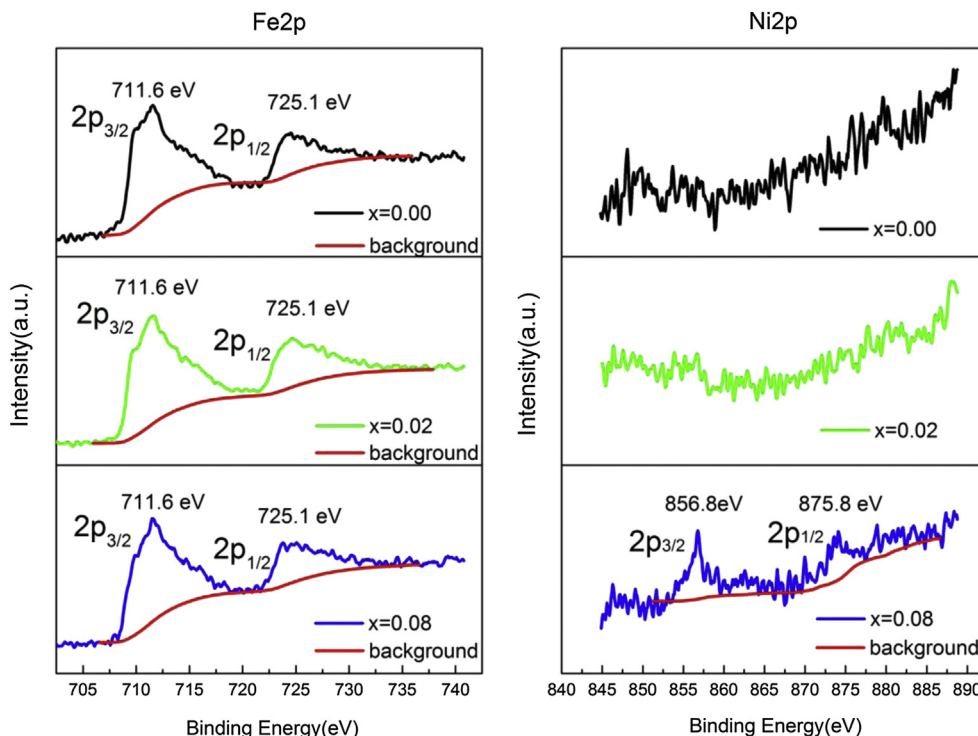


Fig. 4. XPS spectra of $\text{Fe}2\text{p}$ and $\text{Ni}2\text{p}$ core level of $\text{Li}_2\text{Fe}_{1-x}\text{Ni}_x\text{P}_2\text{O}_7/\text{C}$ ($x = 0.00, 0.02$ and 0.08).

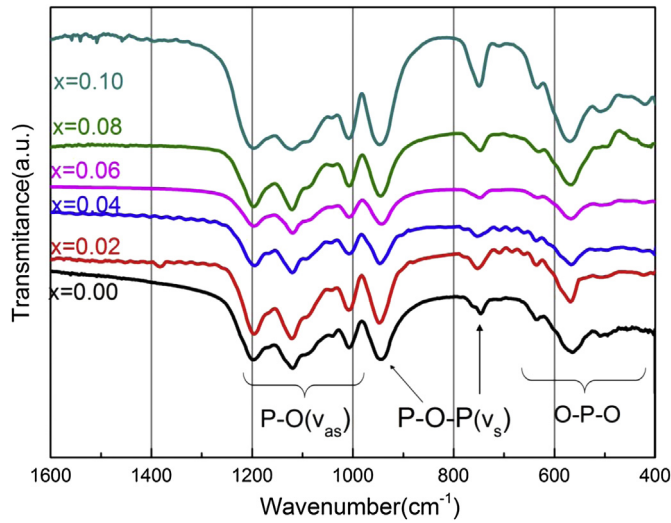


Fig. 5. The FTIR spectroscopy of $\text{Li}_2\text{Fe}_{1-x}\text{Ni}_x\text{P}_2\text{O}_7/\text{C}$.

weight loss and two broad endothermic peaks appear at 73.7 °C and 204.1 °C, mainly corresponding to the release of physically absorbed water of the precursor mixture and crystallized water of $\text{FeC}_2\text{O}_4 \cdot 2\text{H}_2\text{O}$, as well as thermal decomposition of LiH_2PO_4 to form

a dimer [26]. The peak at 430.8 °C is assigned to the reaction between FeO and $\text{Li}_2\text{H}_2\text{P}_2\text{O}_7$, which are decomposition products of FeC_2O_4 and LiH_2PO_4 , respectively [27]. With increasing temperature, an obvious weight loss occurs near 580 °C, accompanying one exothermic peak at 564.6 °C in the DSC curve. The weight loss could be related to the combination of reactants to form lithium iron pyrophosphate. However, the other small peak at 709.6 °C corresponds to the formation of iron phosphide, this is inevitable during the process of complete reduction from Fe^{3+} into Fe^{2+} [28], and the detail information will be discussed elsewhere. From the discussion above, it is clear that an appropriate sintering temperature for synthesis of $\text{Li}_2\text{FeP}_2\text{O}_7$ material is between 600 and 700 °C.

XRD patterns of $\text{Li}_2\text{Fe}_{1-x}\text{Ni}_x\text{P}_2\text{O}_7/\text{C}$ with various amounts of Ni doping are shown in Fig. 2a. All the peaks are indexed to a single phase of monoclinic crystal type $\text{Li}_2\text{FeP}_2\text{O}_7$ with space group $P2_1/c$, which is consistent with the references [16,20]. It is clear that no impurity peaks such as LiFeP_2O_7 or Ni-doped compound are detected, indicating the as-prepared composites are pure phase and the structure is unchanged after Ni doping. These sharp peaks in the patterns suggest that the powders are well crystalline, and the absence of carbon peaks in all patterns indicates that the carbon from pyrolysis of glucose is amorphous.

The enlarged patterns shown in Fig. 2b reveal that the Ni-doped $\text{Li}_2\text{Fe}_{1-x}\text{Ni}_x\text{P}_2\text{O}_7/\text{C}$ samples display a slight shift. With the Ni content increasing, the diffraction peaks shift to higher 2θ angles,

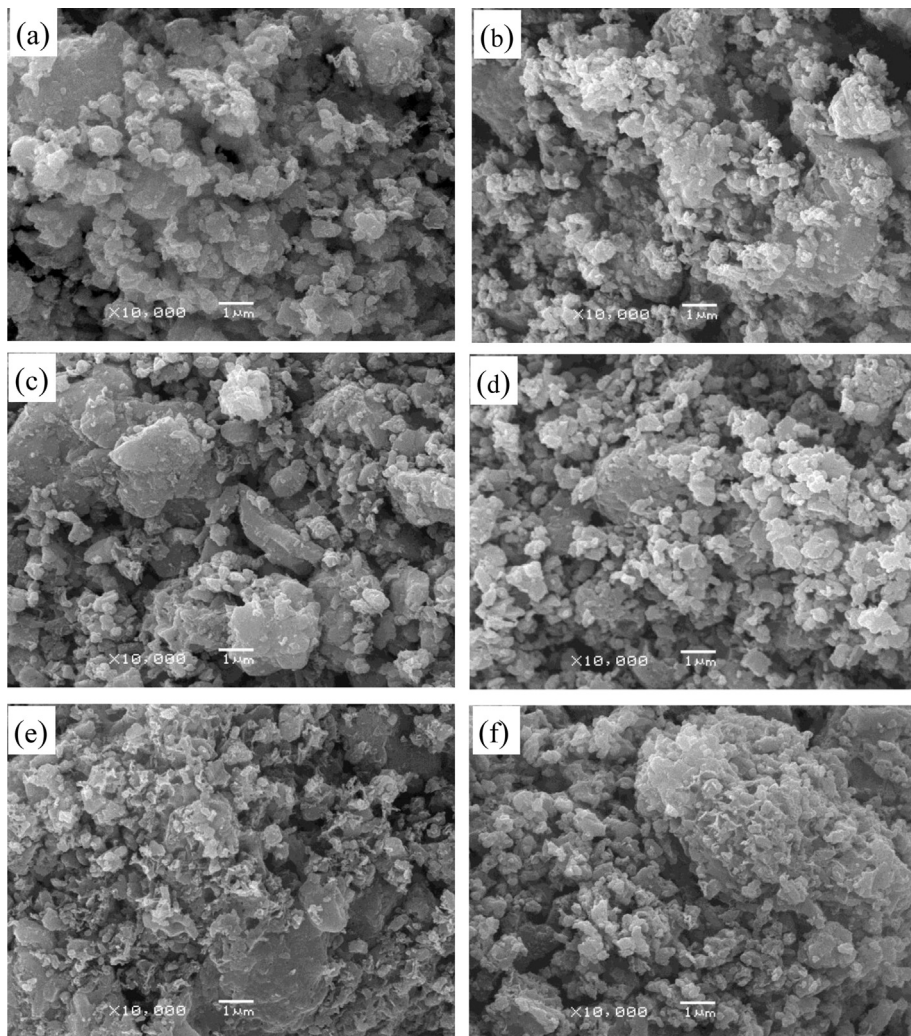


Fig. 6. SEM images of $\text{Li}_2\text{Fe}_{1-x}\text{Ni}_x\text{P}_2\text{O}_7/\text{C}$. (a) $x = 0$; (b) $x = 0.02$; (c) $x = 0.04$; (d) $x = 0.06$; (e) $x = 0.08$ and (f) $x = 0.10$.

which may attribute to the slight difference in ion sizes between nickel ion and iron ion [4].

The XRD patterns of $\text{Li}_2\text{Fe}_{1-x}\text{Ni}_x\text{P}_2\text{O}_7/\text{C}$ ($x = 0, 0.02, 0.04, 0.08$ and 0.10) are refined, as shown in Fig. 3. The calculated results of lattice parameters are listed in Table 1. It can be seen that the observed patterns and calculated patterns match very closely. The $\text{Li}_2\text{FeP}_2\text{O}_7$ sample has similar cell parameters ($a = 11.0329(8)$ Å, $b = 9.7601(5)$ Å, $c = 9.8166(9)$ Å, $\beta = 101.54(4)$, volume = 1035.705 Å) to those reported previously [11]. It can be seen that the values of unit cell parameters a , b , c and volume are

decreased with increasing doping content, indicating Fe ions in the lattice are partially replaced by Ni ions. The smaller radius of Ni^{2+} ion (0.69 Å) than that of Fe^{2+} (0.78 Å) leads to the shrinkage of lattice parameters [29]. This indicates that Ni has been successfully doped into the M1 (Li) or M2 (Fe) sites without affecting the monoclinic structure, which is similar to Co^{2+} doping in $\text{Li}_2\text{FeP}_2\text{O}_7$ [22] and Ni^{2+} doping in LiFePO_4 [30].

Fig. 4 shows the $\text{Fe}2\text{p}$ and $\text{Ni}2\text{p}$ XPS spectra of the pristine $\text{Li}_2\text{FeP}_2\text{O}_7/\text{C}$ and Ni-doped $\text{Li}_2\text{Fe}_{1-x}\text{Ni}_x\text{P}_2\text{O}_7/\text{C}$ ($x = 0.02$ and 0.08). As shown in Fig. 4, the XPS spectra of $\text{Fe}2\text{p}$ in the samples all have two

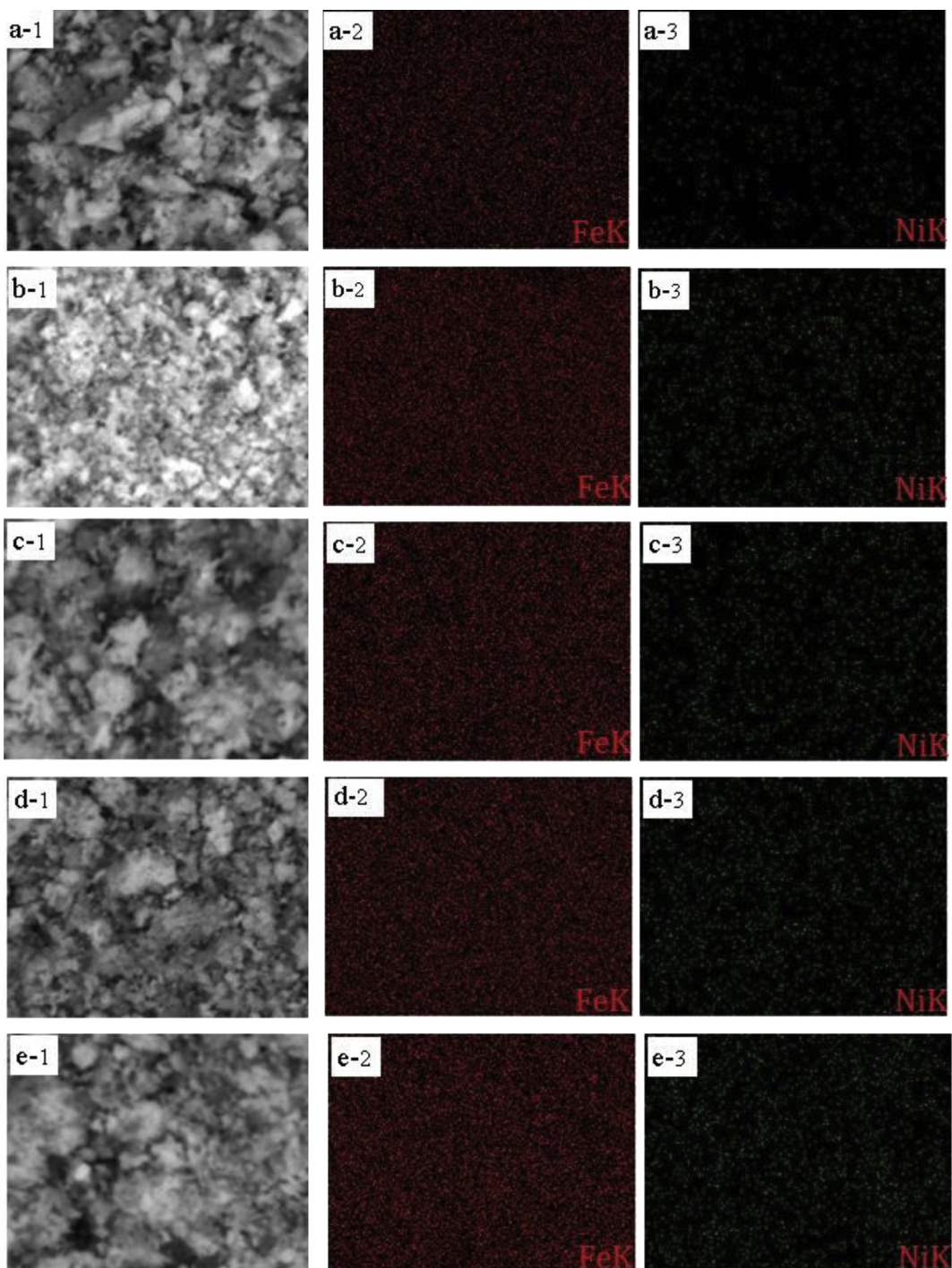


Fig. 7. EDS mappings of the $\text{Li}_2\text{Fe}_{1-x}\text{Ni}_x\text{P}_2\text{O}_7/\text{C}$ powders $x = 0.02$ (a-1, a-2, a-3), $x = 0.04$ (b-1, b-2, b-3), $x = 0.06$ (c-1, c-2, c-3), $x = 0.08$ (d-1, d-2, d-3), $x = 0.10$ (e-1, e-2, e-3).

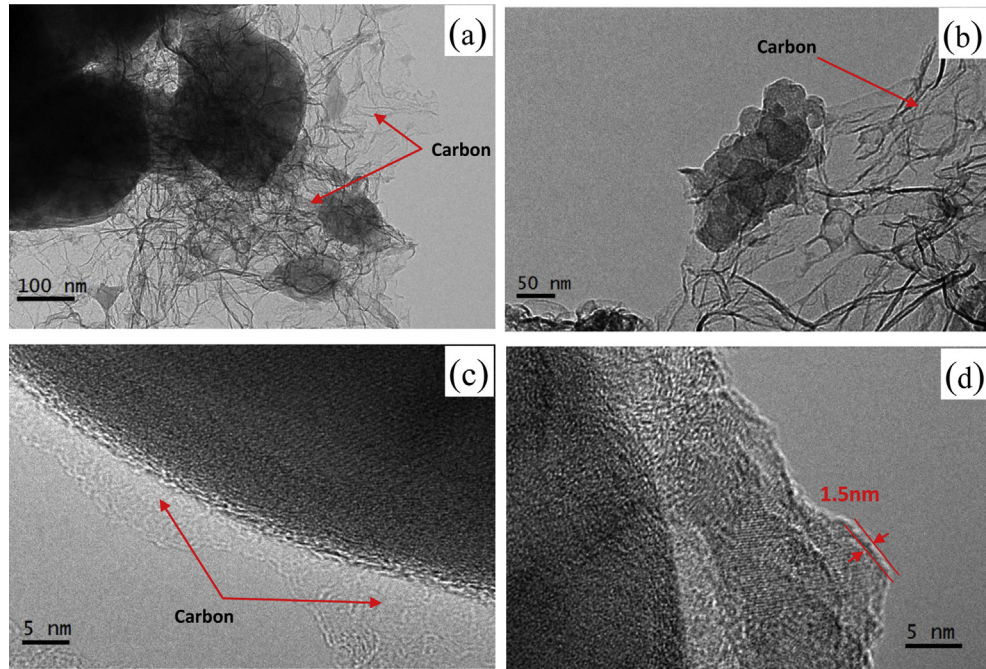


Fig. 8. TEM and HRTEM images of the Li₂FeP₂O₇/C (a, c) and Li₂Fe_{0.98}Ni_{0.02}P₂O₇/C (b, d).

peaks that form the major peak at around 711.6 eV and the satellite peak at 725.1 eV, which can be assigned to Fe2p_{3/2} and Fe2p_{1/2}, respectively, indicating that the oxidation state of Fe is +2 and it is in accordance with the literature values [15,31]. As seen from the corresponding Ni2p spectra in Fig. 4, the peaks at 856.8 eV and 875.8 eV observed in sample Li₂Fe_{0.92}Ni_{0.08}P₂O₇/C are attributed to Ni2p_{3/2} and Ni2p_{1/2}, respectively, which indicates that the oxidation state of Ni is +2, matching well with existing results [32,33]. No peaks can be observed in the Ni2p spectrum of pristine Li₂FeP₂O₇/C, which shows the matrix-doping of Ni into Li₂FeP₂O₇/C lattice and the homogeneous dispersion of Ni among Li₂FeP₂O₇/C.

The details of the chemical bonding in the Li₂Fe_{1-x}Ni_xP₂O₇/C samples are investigated in the Fourier transform infrared (FTIR) spectra as shown in Fig. 5. The FTIR spectra exhibits many prominent and narrow multiple vibration bands in the range of 400–1600 cm⁻¹. The peaks around 500–680 cm⁻¹ are attributed to characteristic bending modes for O—P—O bonds in the PO₄ groups. Meanwhile, the peaks observed at about 745 and 945 cm⁻¹ are assigned to the symmetric and asymmetric P—O—P vibrations and the peaks in the range of 1000–1200 cm⁻¹ correspond to the P—O stretching vibrational frequencies. The weak peaks in the region of 1400–1600 cm⁻¹ are related to the absorbance of the residual carbon [34]. However, the characteristic peaks of NiO (production of Ni(CH₃COO)₂·4H₂O) are approximately 450 and 562 cm⁻¹ [35] not found in Fig. 5, indicating that the Ni was incorporated into the lattice of Li₂FeP₂O₇ successfully. All these similarities of the vibrational spectra for P—O—P, O—P—O and PO₃ bonds in (P₂O₇)⁴⁻, were observed in the FTIR spectra for all samples and are precisely indexed with the typical vibration of pyrophosphate groups, that have been consistent with previous reports [15,16,22]. Besides, the results are in accordance with the XRD refinement results.

The SEM images of Li₂Fe_{1-x}Ni_xP₂O₇/C ($x = 0.00, 0.02, 0.04, 0.06, 0.08, 0.10$) powders are shown in Fig. 6. It is observed that the primary particles are nano-scaled and agglomerated to form secondary particles, showing similar irregular granular shapes. There is no obvious change in morphologies after Ni²⁺ doping.

The EDS mappings illustrate the element mapping of Fe and Ni in the doped samples as shown in Fig. 7. It shows that the element

Fe is homogeneously distributed in the particles, while the mapping dense of Ni gradually increases with the rise of Ni concentrations, indicating that the precursors of Fe and Ni were blended uniformly at molecular level during preparation, even for doping ions at a low content. The TEM images of Li₂Fe_{1-x}Ni_xP₂O₇/C ($x = 0.00$ and 0.02) are illustrated in Fig. 8. It can be seen that the Li₂Fe_{1-x}Ni_xP₂O₇/C particles are coated with nano carbon-webs. Fig. 8(d) shows that the thickness of layer of nano-carbon is approximately 1.5 nm, which provides short diffusion lengths and enhances conductivity [31].

Fig. 9 shows the initial charge–discharge profiles of Li₂Fe_{1-x}Ni_xP₂O₇/C ($x = 0.00, 0.02, 0.04, 0.06, 0.08, 0.10$) cathodes at 0.025C. All the charge–discharge profiles have two flat voltage plateaus at around 3.5 V and 3.8 V, which attribute to the main characteristic of the two-phase manner based on the redox couple of Fe²⁺/Fe³⁺ during lithium-ion extraction and insertion between

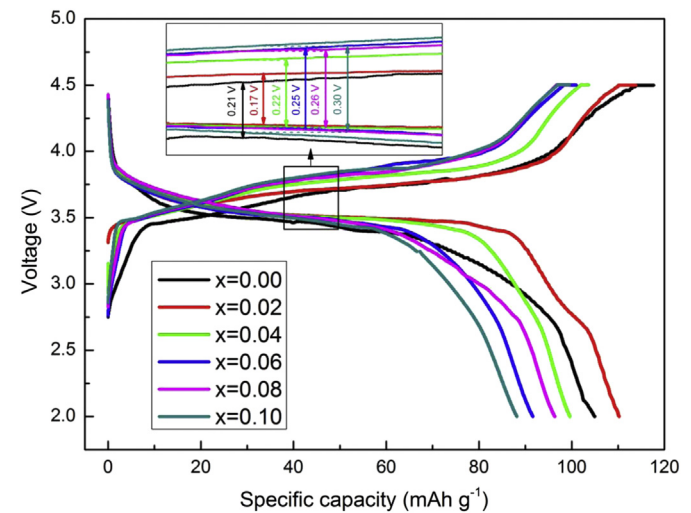


Fig. 9. Initial charge–discharge profile of the Li₂Fe_{1-x}Ni_xP₂O₇/C at 0.025C.

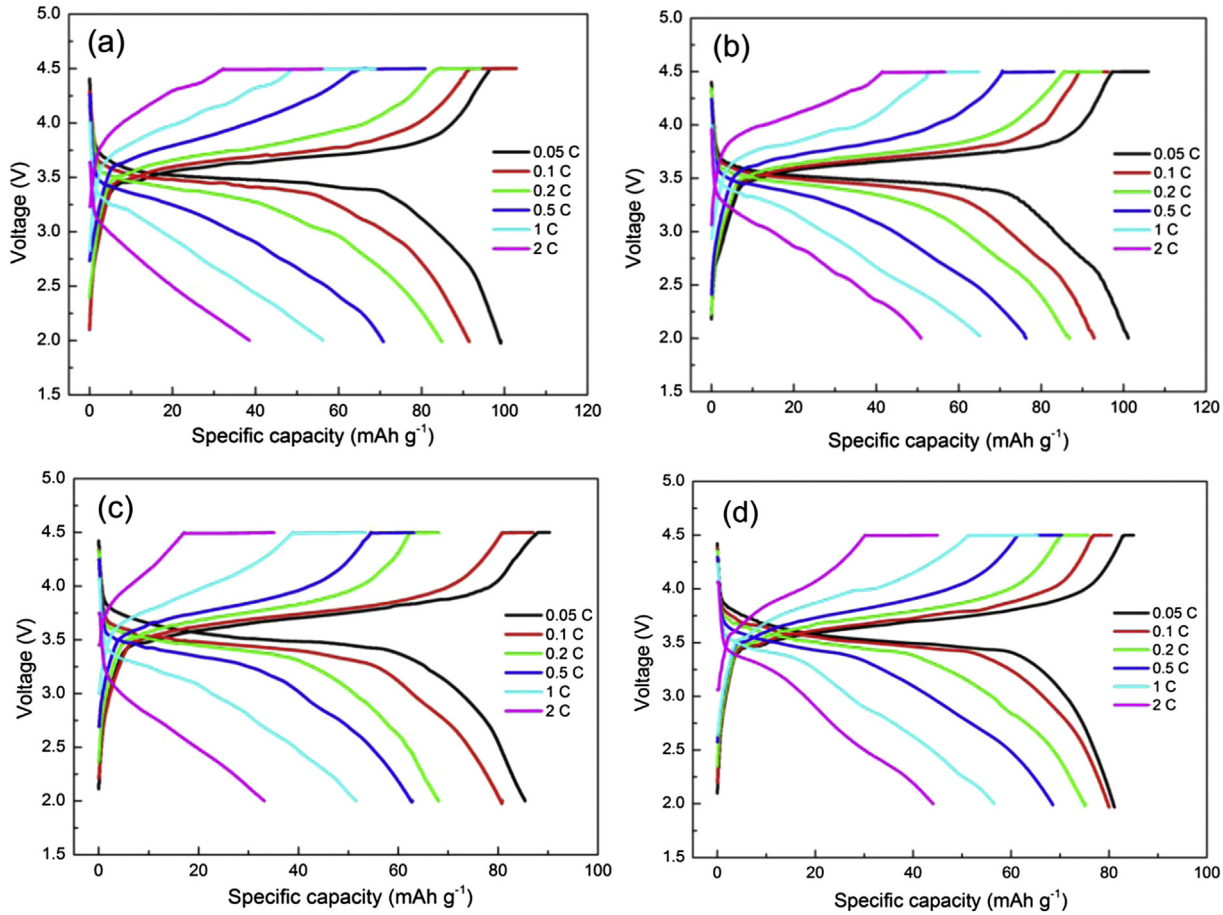


Fig. 10. Electrochemical charge–discharge curves of $\text{Li}_2\text{Fe}_{1-x}\text{Ni}_x\text{P}_2\text{O}_7/\text{C}$ at various rates (a) $x = 0$, (b) $x = 0.02$, (c) $x = 0.06$, (d) $x = 0.10$.

$\text{Li}_2\text{FeP}_2\text{O}_7$ and LiFeP_2O_7 [13]. It can be seen that the discharge plateaus of Ni-doped samples are much higher than that of the pristine one, as illustrated in inset of Fig. 9. This indicates that the $\text{Fe}^{2+}/\text{Fe}^{3+}$ redox potential could be raised above 3.5 V by partial Ni substitution, this is in accordance with the results of other transition metal doping [20,36]. The discharge specific capacities of $\text{Li}_2\text{Fe}_{1-x}\text{Ni}_x\text{P}_2\text{O}_7/\text{C}$ composites with $x = 0, 0.02, 0.04, 0.06, 0.08, 0.10$ are 105.0, 110.2, 99.6, 91.3, 96.4 and 88.2 mAh g^{-1} , respectively. The columbic efficiency of the initial cycle is about 94.6%, 99.3%, 97.6%, 93.2%, 97.4%, and 92.8%, respectively. It can be observed that $\text{Li}_2\text{Fe}_{0.98}\text{Ni}_{0.02}\text{P}_2\text{O}_7/\text{C}$ clearly exhibits best electrochemical performance with the lowest polarization potential (0.17 V) and highest initial discharge capacity, indicating that Ni-doping does not block the tunnels of Li ions and probably increases the charge and discharge capacities and charge–discharge efficiency.

The charge–discharge profiles of the $\text{Li}_2\text{Fe}_{1-x}\text{Ni}_x\text{P}_2\text{O}_7/\text{C}$ ($x = 0, 0.02, 0.06, 0.10$) at various rates, from 0.05 to 2C, are shown in Fig. 10. The rate performance of the composites is highly affected by the nickel-doped content. Increasing Ni-doping amount first led to the enhancement of rate capability. The sample of $\text{Li}_2\text{Fe}_{0.98}\text{Ni}_{0.02}\text{P}_2\text{O}_7$ exhibits the best rate performance, it can deliver a capacity of 102.3 mAh g^{-1} at 0.05C, 78.5 mAh g^{-1} at 0.5C and 64.7 mAh g^{-1} at 1C. Moreover, the discharge voltage plateau of sample $\text{Li}_2\text{Fe}_{0.98}\text{Ni}_{0.02}\text{P}_2\text{O}_7$ is still higher than 3.2 V at 1C rate, indicating that $\text{Li}_2\text{Fe}_{0.98}\text{Ni}_{0.02}\text{P}_2\text{O}_7$ has a lower polarization. However, when the Ni-doping content is increased further, the discharge capacity will decrease at all rates as presented from Fig. 10(c) to (d), which could be ascribed by two factors: it is difficult

to trigger a 2-electron reaction for $\text{Li}_2\text{FeP}_2\text{O}_7$ even with Ni doping, is assumed that this occurs at high voltage of 5.2 V. On the other side, the presence of excessive Ni^{2+} is redox inactive with the capacity contribution mostly coming from existing Fe in the composite [20,36]. A similar phenomenon has been reported to occur on Ni-doped LiFePO_4 [37,38] and $\text{Li}_3\text{V}_2(\text{PO}_4)_3$ [39].

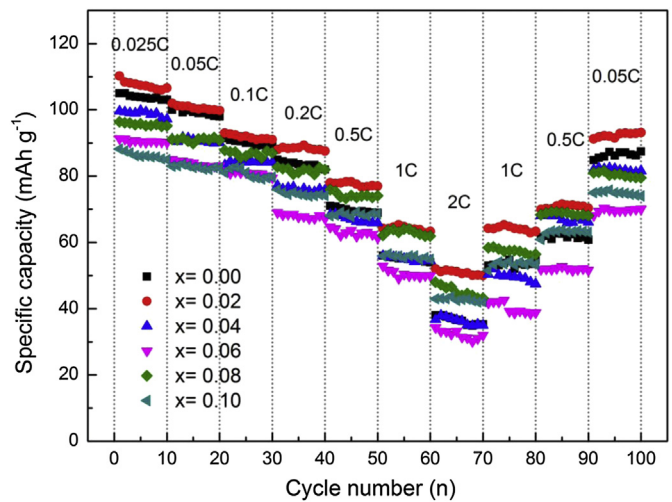


Fig. 11. Cycling performances of $\text{Li}_2\text{Fe}_{1-x}\text{Ni}_x\text{P}_2\text{O}_7/\text{C}$ at different rates.

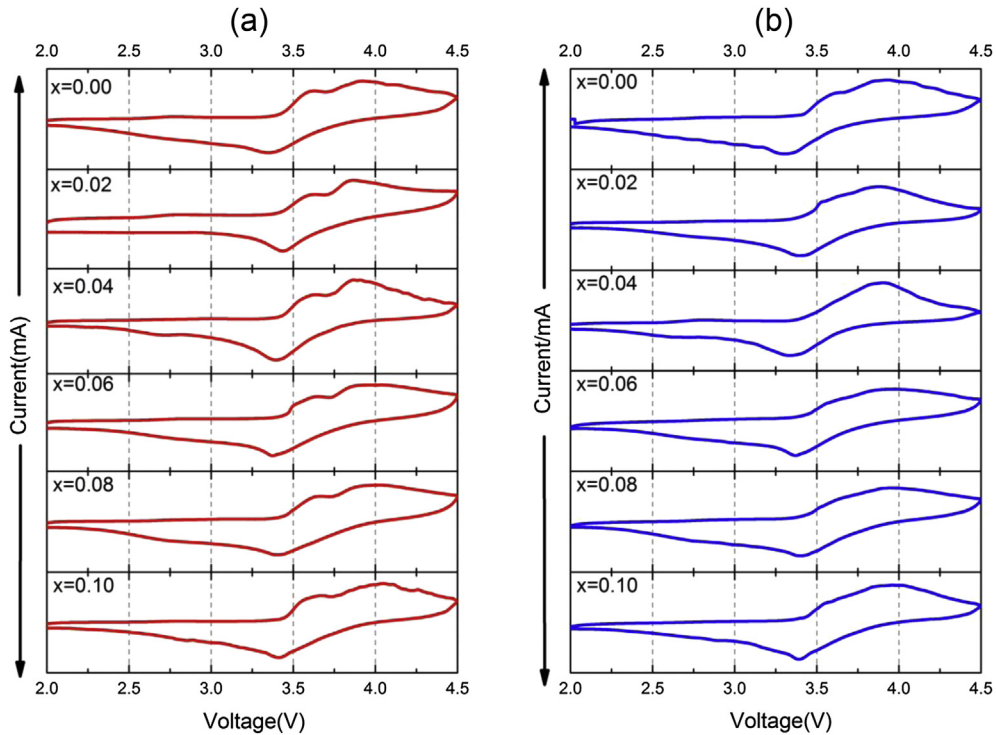


Fig. 12. Cyclic voltammograms of $\text{Li}_2\text{Fe}_{1-x}\text{Ni}_x\text{P}_2\text{O}_7/\text{C}$ electrodes (a) the first cycle, (b) the second cycle.

The cycling performances of $\text{Li}_2\text{Fe}_{1-x}\text{Ni}_x\text{P}_2\text{O}_7/\text{C}$ ($x = 0.00, 0.02, 0.04, 0.06, 0.08$ and 0.10) are compared in Fig. 11. The rate performance of $\text{Li}_2\text{Fe}_{0.98}\text{Ni}_{0.02}\text{P}_2\text{O}_7/\text{C}$ demonstrates the best among all samples, it keeps a capacity retention ratio of about 97.5% at all rates, higher than that of the others. The sample with suitable Ni-doped content ($x = 0.02$) shows excellent rate performance compared with other samples, corresponding to a capacity retention of 90.1% at 0.05C after 100 cycles.

To provide more information about the electrochemical property, the first two cyclic voltammograms (CV) of Ni doped $\text{Li}_2\text{FeP}_2\text{O}_7/\text{C}$ samples in the voltage range of 2.0–4.5 V are presented in Fig. 12. In the first cycle under a scanning rate of 0.1 mV s^{-1} , two high intensity anodic peaks appear during negative scanning, coupled with only one clear cathodic peak in positive scanning, these correspond to the “splitting” of Fe in the redox reaction [18]. The weak peak at 4.5 V is still mystery, it could not be explained by electrochemical theory, nor approved by electrolyte decomposition [15,16]. In the second cycle, it is noticeable that the two anodic peaks merged into one centered peak for all samples. However, the lithium extraction and insertion processes for Ni doped samples are more stable, which is ascribed to relatively sharper peaks and a higher potential. The reason could be that some irreversible structural disorder in pyrophosphate system (two octahedral sites of Fe have an edge-sharing configuration in the triplite structure) could be suppressed by substituting some transition metal [40–42]. Meanwhile, it is apparent that the redox potentials slightly shift to a higher potential as the amount of Ni doping is increased, especially for the high anodic peak, it can reach a potential as high as 3.95 V without the combination of hygroscopic anions as SO_4^{2-} or F^- [43,44], which is the highest $\text{Fe}^{3+}/\text{Fe}^{2+}$ redox potential in phosphate materials. A similar phenomenon about the Fe-peak upshift has been reported in the case of the other metal-doping materials, such as $\text{Li}_2\text{Fe}_{1-x}\text{Mn}_x\text{P}_2\text{O}_7$ and $\text{Li}_2\text{Fe}_{1-x}\text{Co}_x\text{P}_2\text{O}_7$.

Fig. 13(a) shows the impedance spectra curves of the $\text{Li}_2\text{Fe}_{1-x}\text{Ni}_x\text{P}_2\text{O}_7/\text{C}$ ($x = 0.00, 0.02, 0.04, 0.06, 0.08$ and 0.10) composites.

All curves exhibit a semicircle in the high frequency region and a straight inclined line in the low frequency region, these correspond to the charge-transfer resistance at the cathode/electrolyte interface and the diffusion of the lithium ions into the bulk of electrode material, respectively. The impedance spectra are fitted by using the equivalent electrical circuit model as shown in inset of Fig. 13(a), where R_s corresponds to the solvent resistance and R_{ct} stands for charge-transfer resistance, CPE relates to the double layer capacitance and passivation film capacitance and Z_w is the Warburg impedance [45] which is associated with lithium-ion diffusion in the $\text{Li}_2\text{FeP}_2\text{O}_7$ particles. The obtained R_{ct} of $\text{Li}_2\text{Fe}_{0.98}\text{Ni}_{0.02}\text{P}_2\text{O}_7/\text{C}$ is 107.3Ω , which is obviously the smallest among the samples listed in Table 2, indicating that the transfer and diffusion of Li^+ through the cathode/electrolyte interface of $\text{Li}_2\text{Fe}_{1-x}\text{Ni}_x\text{P}_2\text{O}_7/\text{C}$ is easier than other samples.

To further investigate the electrochemical performance of the samples, a plot of real impedance versus inverse square root of the lower angular frequency $\omega^{-0.5}$ is shown in Fig. 13(b), from which the value of Warburg impedance coefficient (σ_w) can be obtained according to Eq. (1) [46].

$$Z' = R_s + R_{ct} + \sigma_w \omega^{-0.5} \quad (1)$$

where R_s is the resistance of solvent, R_{ct} is the charge transfer resistance and ω is the angular frequency. Both R_s and R_{ct} are independent of frequency. Meanwhile, the lithium ion diffusion coefficient (D_{Li}) can be used to measure the kinetics activity for an electrochemical reaction, which can be roughly presented by the following Eq. (2) [47,48]

$$D_{\text{Li}} \propto 1/\sigma_w^2 \quad (2)$$

It is obviously shown that the squared value of σ_w is reciprocally proportional to the D_{Li} value. Therefore, the lithium ion diffusion of samples can be speculated by the value of σ_w indirectly. The

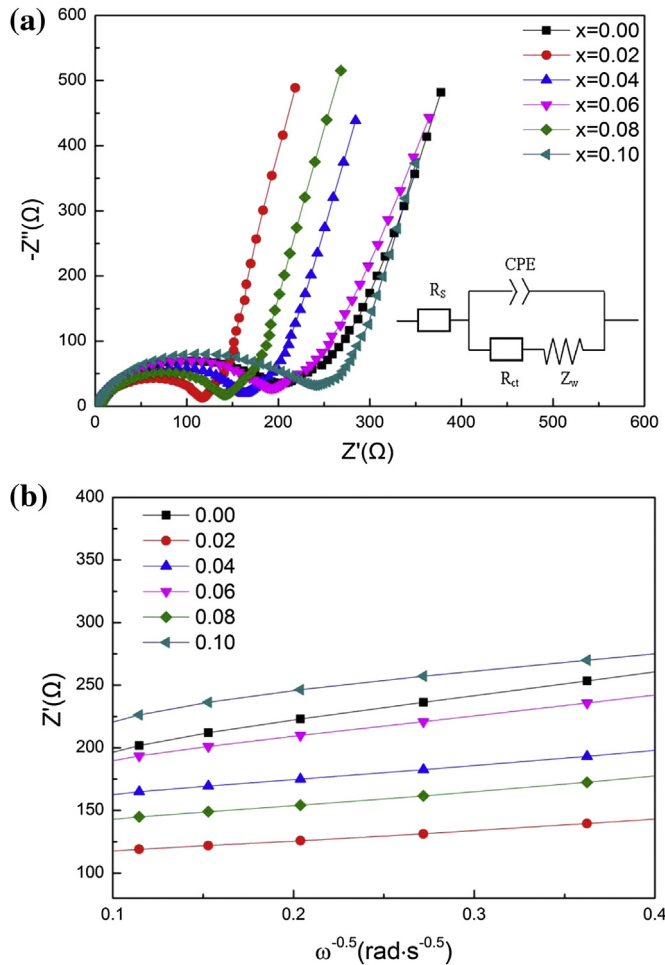


Fig. 13. (a)The impedance spectra of $\text{Li}_2\text{FeP}_2\text{O}_7/\text{C}$ and $\text{Li}_2\text{Fe}_{1-x}\text{Ni}_x\text{P}_2\text{O}_7/\text{C}$. (b) The relationship between real impedance (Z') and the inverse of square root of angular frequency ($\omega^{-0.5}$) in low frequency region.

Table 2
Result of electrochemical impedance and Warburg impedance coefficient.

Samples	$R_s \Omega^{-1}$	$R_{ct} \Omega^{-1}$	Z_w	$\sigma \Omega^{-1} \text{s}^{-0.5}$
$\text{Li}_2\text{FeP}_2\text{O}_7/\text{C}$	2.358	163.0	123.1	210.38
$\text{Li}_2\text{Fe}_{0.98}\text{Ni}_{0.02}\text{P}_2\text{O}_7/\text{C}$	2.821	107.3	22.64	83.06
$\text{Li}_2\text{Fe}_{0.96}\text{Ni}_{0.04}\text{P}_2\text{O}_7/\text{C}$	4.331	155.8	11.48	113.74
$\text{Li}_2\text{Fe}_{0.94}\text{Ni}_{0.06}\text{P}_2\text{O}_7/\text{C}$	3.131	165.1	71.73	169.82
$\text{Li}_2\text{Fe}_{0.92}\text{Ni}_{0.08}\text{P}_2\text{O}_7/\text{C}$	5.524	129.0	25.11	111.27
$\text{Li}_2\text{Fe}_{0.90}\text{Ni}_{0.10}\text{P}_2\text{O}_7/\text{C}$	2.065	191.4	150	176.96

calculated values of σ_w for $\text{Li}_2\text{Fe}_{1-x}\text{Ni}_x\text{P}_2\text{O}_7/\text{C}$ composites are listed in Table 2. It is seen that $\text{Li}_2\text{Fe}_{0.98}\text{Ni}_{0.02}\text{P}_2\text{O}_7/\text{C}$ exhibit the smallest value of σ_w among all the samples, presenting the highest value lithium ion diffusion coefficient. It indicates that the electrochemical property of $\text{Li}_2\text{FeP}_2\text{O}_7/\text{C}$ composites can be improved by an appropriate amount of Ni ion doping.

4. Conclusion

The well crystallized $\text{Li}_2\text{Fe}_{1-x}\text{Ni}_x\text{P}_2\text{O}_7/\text{C}$ ($x = 0.00, 0.02, 0.04, 0.06, 0.08$ and 0.10) composites are successfully prepared via solid-state route. Based on the XRD refinement results, Ni^{2+} has incorporated into the lattice of $\text{Li}_2\text{FeP}_2\text{O}_7$ and all the Ni^{2+} -doped composites can be indexed to a monoclinic structure with space

group $P2_1/c$. The amount of Ni doping has an important impact on electrochemical performance. The $\text{Li}_2\text{Fe}_{0.98}\text{Ni}_{0.02}\text{P}_2\text{O}_7/\text{C}$ shows the best cycling stability and rate capability among all the samples, having the highest discharge capacity of 110.2 mAh g^{-1} at 0.025C , and possessing the capacity retention of 90.1% after 100 cycles at 0.05C . The results of CV and EIS revealed that the doping nickel at an appropriate amount could increase the diffusion coefficient of lithium ions and result in the improvement of the reversibility of the materials. The results indicate that the Ni doping is an effective approach to achieve excellent electrochemical performance for the lithium ion pyrophosphate.

Acknowledgment

This study was supported by National Natural Science Foundation of China (501100001809) (Grant No.51302324).

References

- [1] M. Armand, J.M. Tarascon, *Nature* 451 (2008) 652–657.
- [2] Z. Liang, Y. Zhao, *Electrochim. Acta* 94 (2013) 374–380.
- [3] J.-c. Zheng, X.-h. Li, Z.-x. Wang, H.-j. Guo, S.-y. Zhou, *J. Power Sources* 184 (2008) 574–577.
- [4] Q. Liu, Z. Liu, G. Xiao, S. Lia, *Ionics* 19 (2013) 445–450.
- [5] J.-c. Zheng, X.-h. Li, Z.-x. Wang, S.-s. Niu, D.-r. Liu, L. Wu, L.-j. Li, J.-h. Li, H.-j. Guo, *J. Power Sources* 195 (2010) 2935–2938.
- [6] T. Muraligand, K.R. Stroukoff, A. Manthiram, *Chem. Mater.* 22 (2010) 5754–5761.
- [7] L. Tao, J.R. Neilson, B.C. Melot, T.M. McQueen, C. Masquelier, G. Rousse, *Inorg. Chem.* 52 (2013) 11966–11974.
- [8] R. Tripathi, G. Popov, X. Sun, D.H. Ryan, L.F. Nazar, *J. Mater. Chem. A* 1 (2013) 2990–2994.
- [9] X. Qiao, J. Yang, Y. Wang, Q. Chen, T. Zhang, L. Liu, X. Wang, *J. Solid State Electrochem.* 16 (2012) 1211–1217.
- [10] C.V. Subban, M. Atti, G. Rousse, A.M. Abakumov, G.V. Tendeloo, R. Janot, J.-M. Tarascon, *J. Am. Chem. Soc.* 135 (2013) 3653–3661.
- [11] S.-i. Nishimura, M. Nakamura, R. Natsui, A. Yamada, *J. Am. Chem. Soc.* 132 (2010) 13596–13597.
- [12] P. Barpanda, S.-i. Nishimura, A. Yamada, *Adv. Energy Mater.* 2 (2012) 841–859.
- [13] D. Shimizu, S.-i. Nishimura, P. Barpanda, A. Yamada, *Chem. Mater.* 24 (2012) 2598–2603.
- [14] J.M. Clark, S.-i. Nishimura, A. Yamada, M.S. Islam, *Angew. Chem. Int. Ed.* 51 (2012) 13149–13153.
- [15] Juan Du, Lifang Jiao, Qiong Wu, Yongchang Liu, Yanping Zhao, Lijing Guo, Yijng Wang, Huatang Yuan, *Electrochim. Acta* 103 (2013) 219–225.
- [16] H. Zhou, S. Upadhyay, N.A. Chernova, G. Hautier, G. Ceder, M.S. Whittingham, *Chem. Mater.* 23 (2011) 293–300.
- [17] P. Barpanda, T. Ye, S.-C. Chung, Y. Yamada, S.-i. Nishimura, A. Yamada, *J. Mater. Chem.* 22 (2012) 13455–13459.
- [18] M. Tamaru, P. Barpanda, Y. Yamada, S.-i. Nishimura, A. Yamada, *J. Mater. Chem.* 22 (2012) 24526–24529.
- [19] G. Hautier, A. Jain, T. Mueller, C. Moore, S.P. Ong, G. Ceder, *Chem. Mater.* 25 (2013) 2064–2074.
- [20] N. Furuta, S.-i. Nishimura, P. Barpanda, A. Yamada, *Chem. Mater.* 24 (2012) 1055–1061.
- [21] H. Zhou, S. Upadhyay, Natasha A. Chernova, M.S. Whittingham, *Acta Crystallogr.* 67 (2011) 58–59.
- [22] H. Kim, S. Lee, Y.-U. Park, H. Kim, J. Kim, S. Jeon, K. Kang, *Chem. Mater.* 23 (2011) 3930–3937.
- [23] M.J. Mahesh, G.S. Gopalakrishna, K.G. Ashamanjari, *Mater. Sci. Semicond. Process* 10 (2007) 117–123.
- [24] Y.-H. Kao, M. Tang, N. Meethong, J. Bai, W.C. Carter, Y.-M. Chiang, *Chem. Mater.* 22 (2010) 5845–5855.
- [25] L. Lin, Y. Wen, O. J. Y. Guo, D. Xiao, *RSC Adv.* 3 (2013) 14652–14660.
- [26] S.S. Zhang, J.L. Allen, K. Xu, T.R. Jow, *J. Power Sources* 147 (2005) 234–240.
- [27] A. Liu, Y. Liu, Z. Hu, G. Gao, Y. Xu, L. Lei, *J. Phys. Chem. Solids* 72 (2011) 831–835.
- [28] V. Drozd, G.Q. Liu, R.S. Liu, H.T. Kuo, C.H. Shen, D.S. Shy, X.K. Xing, *J. Alloys Compd.* 487 (2009) 58–63.
- [29] W.K. Zhang, Y.L. Hu, X.Y. Tao, H. Huang, Y.P. Gan, C.T. Wang, *J. Phys. Chem. Solids* 71 (2010) 1196–1200.
- [30] A. Öner, E. Bulut, M. Can, M.t Özçar, *J. Solid State Electrochem.* 17 (2013) 3101–3107.
- [31] Y. Ge, X. Yan, J. Liu, X. Zhang, J. Wang, X. He, R. Wang, H. Xie, *Electrochim. Acta* 55 (2010) 5886–5890.
- [32] J.P. Cheng, B.B. Wang, M.G. Zhao, F. Liu, X.B. Zhang, *Sens. Actuators B* 190 (2014) 78–85.
- [33] M. Sun, Z. Chen, J. Yu, *Electrochim. Acta* 109 (2013) 13–19.

- [34] H.-M. Xie, R.-S. Wang, J.-R. Ying, L.-Y. Zhang, A.F. Jalbout, H.-Y. Yu, G.-L. Yang, X.-M. Pan, Z.-M. Su, *Adv. Mater.* 18 (2006) 2609–2613.
- [35] M.A. Gondal, T.A. Saleh, Q.A. Drmosh, *Appl. Surf. Sci.* 258 (2012) 6982–6986.
- [36] T. Ye, P. Barpanda, S.-i. Nishimura, N. Furuta, S.-C. Chung, A. Yamada, *Chem. Mater.* 25 (2013) 3623–3629.
- [37] Y. Lu, J. Shi, Z. Guo, Q. Tong, W. Huang, B. Li, *J. Power Sources* 194 (2009) 786–793.
- [38] D. Wang, H. Li, S. Shi, X. Huang, L. Chen, *Electrochim. Acta* 50 (2005) 2955–2958.
- [39] Y. Zhang, Q-y. Huo, Y. Lv, L-z. Wang, A-q. Zhang, Y-h. Song, G-y. Li, H-l. Gao, T-c. Xia, H-c. Dong, *J. Alloys Compd.* 542 (2012) 187–191.
- [40] R. Malik, F. Zhou, G. Ceder, *Phys. Rev. B* 79 (2009) 214201–214207.
- [41] S. Lee, S.S. Park, *Chem. Mater.* 24 (2012) 3550–3557.
- [42] G. Hautier, A. Jain, S.P. Ong, B. Kang, C. Moore, R. Doe, G. Ceder, *Chem. Mater.* 23 (2011) 3495–3508.
- [43] N. Recham, J.-N. Chotard, L. Dupont, C. Delacourt, W. Walker, M. Armand, J.-M. Tarascon, *Nat. Mater.* 9 (2010) 68–74.
- [44] S.C. Chung, P. Barpanda, S.-i. Nishimura, Y. Yamadaa, A. Yamada, *Phys. Chem. Chem. Phys.* 14 (2012) 8678–8682.
- [45] Z. Yan, S. Cai, L. Miao, X. Zhou, Y. Zhao, *J. Alloys Compd.* 511 (2012) 101–106.
- [46] Z.-Q. Huo, Y.-T. Cui, D. Wang, Y. Dong, L. Chen, *J. Power Sources* 245 (2014) 331–336.
- [47] B. Jin, E.M. Jin, K.-H. Park, H.-B. Gu, *Electrochem. Commun.* 10 (2008) 1537–1540.
- [48] X. Zhou, C. Cui, G. Wu, H. Yang, J. Wu, J. Wang, G. Gao, *J. Power Sources* 238 (2013) 95–102.